AIAA SciTech Forum
23-27 January 2023, National Harbor, MD & Online
AIAA SCITECH 2023 Forum

10.2514/6.2023-1042

Three-Dimensional Receptivity of a Hypersonic Straight Cone Boundary Layer to a Freestream Vorticity Disturbance

Anand R. Varma*
University of California, Los Angeles, California, 90095, USA

Carleton P. Knisely†
Lawrence Livermore National Laboratory, Livermore, California, 94550, USA

Xiaolin Zhong‡
University of California, Los Angeles, California, 90095, USA

Three-dimensional receptivity is relevant to transition prediction in scenarios where freestream disturbances are highly three-dimensional, such as atmospheric turbulence in free flight. The straight cone at zero angle of attack is a typical flow configuration, but as very few studies have considered three-dimensional receptivity for this configuration, the knowledge base is limited. The objective of this study is to expand on the existing knowledge base by investigating the three-dimensional receptivity of an axisymmetric straight cone boundary layer to a freestream vorticity disturbance. The configuration is a Mach 15 flow over a 0.5-mm-nose-radius straight cone at an altitude of 26 km and at zero angle of attack. The freestream vorticity disturbance is composed of three oblique planar vorticity waves, each with a different axial wavelength (corresponding to different frequencies) but with the same vertical wavelength, which is kept the same to ensure similar azimuthal wavenumber spectra. An unsteady direct numerical simulation (DNS) is performed to simulate the boundary-layer receptivity process. In the leading-edge receptivity region (upstream of second-mode amplification), and for the waves corresponding to the two lower frequencies (400 kHz and 800 kHz), the results indicate an extended forcing region for the oblique components of the boundary-layer disturbance when compared to the 2-D components. However, the oblique components also feature smaller overall amplitudes in this region. For the wave corresponding to a frequency of 1200 kHz, similar observations could not be made, but the oblique components are found to generally attain smaller amplitudes after second-mode growth in comparison to the 2-D component.

I. Introduction

Predicting laminar-to-turbulent transition in the boundary layer is critical to the design of hypersonic vehicles, as surface heating and drag are much higher in a turbulent flow compared to a laminar flow. Transition to turbulence is ultimately caused by environmental disturbances, such as freestream disturbances or surface roughness. There are several paths by which an environmental disturbance causes transition, and the specific path taken by a disturbance depends on its initial amplitude. The current study is primarily concerned with weak environmental disturbances. In the so-called linear receptivity process, these environmental disturbances generate and excite boundary-layer disturbance modes, which then undergo eigenmode growth through an instability mechanism, the nature of which depends on the flow regime. In two-dimensional (2-D) and axisymmetric hypersonic boundary layers, the predominant boundary-layer instability mechanism is Mack's [1] second mode, which is an inviscid instability associated with trapped acoustic waves within the boundary layer. Through this instability, the boundary-layer disturbance modes can eventually become large enough to induce nonlinear interactions, after which transition to turbulence begins.

In some cases, the freestream disturbances that ultimately lead to transition are highly three-dimensional, for example, atmospheric turbulence in free flight. In these cases, the receptivity process is three-dimensional (3-D), which means the resulting boundary-layer disturbance structure is dependent not only on the wall-tangent and wall-normal directions, but also on the spanwise (in the case of a flat plate) or azimuthal (in the case of an axisymmetric body) directions. In

*Ph.D. Student, Mechanical and Aerospace Engineering, varmaar@ucla.edu
†Computational Engineering Division, knisely2@llnl.gov
‡Professor, Mechanical and Aerospace Engineering, xiaolin@seas.ucla.edu

addition, the receptivity of oblique boundary-layer disturbance modes (modes where the wave vector is not aligned with the streamwise direction) comes into play. While the straight cone at zero angle-of-attack is a typical configuration, very few studies have considered three-dimensional receptivity to freestream disturbances for this configuration.

Balakumar [2] conducted a numerical study on the linear receptivity of a Mach 3.5 straight cone flow to freestream oblique slow acoustic plane waves and found that for a freestream disturbance with fixed spanwise wavelength, the azimuthal spectrum of the boundary-layer disturbance widens with increasing streamwise distance. More recently, Wan *et al.* [3] performed a numerical study on the effect of incidence angle on the linear receptivity of a Mach 6 straight cone flow to oblique freestream slow acoustic plane waves. They found that the boundary-layer disturbance on the leeward side of the cone (the side facing away from the freestream wave) is stronger than on the windward side (the side facing towards the freestream wave). They also found that increasing the incidence angle leads to a stronger wall response on the leeward side and a weaker response on the windward side. Both of these studies focused on receptivity to freestream acoustic waves, which are prevalent in ground test facilities. However, vorticity and entropy waves are expected to be more dominant in free flight, with the former being associated with freestream turbulence.

The objective of this study is to expand on the existing knowledge base by investigating the three-dimensional receptivity of an axisymmetric straight cone boundary layer to a freestream vorticity disturbance. The paper will begin with a description of the simulation conditions and the governing equations. The numerical methods (DNS and LST) will be discussed, and the freestream disturbance model will be described. The steady DNS solution will be briefly described. The LST results will be used to identify and characterize the boundary-layer instabilities. Unsteady DNS is performed to simulate the receptivity of the boundary layer to the aforementioned freestream disturbance. The results will be analyzed based on the behavior of oblique and 2-D boundary-layer disturbances in the resulting boundary-layer response.

II. Simulation Conditions

We consider a Mach 15 flow over a straight cone with a nose radius of 0.5 mm and half-angle of 5 degrees, at zero angle-of-attack. The freestream conditions correspond to atmospheric conditions at an altitude of 26 km (85 kft) and are shown in Table 1. To better approximate wall temperature distributions found in real flight conditions, we use the approach of Mortensen [4]. In the nose region, wall temperatures are computed by assuming radiative equilibrium at the surface, with surface emissivity $\epsilon = 0.8$. On the cone frustum, the temperature is then exponentially lowered to 1000 K. The resulting wall temperature distribution is shown in Fig. 1. The symbol s denotes the arclength along the surface of the cone, measured from the stagnation point. The wall is assumed to be noncatalytic and in thermal equilibrium (i.e. the translation-rotation temperature is set equal to the vibration temperature).

The computational domain extends to $s = 1.8$ m and is discretized using 384 points in the wall-normal direction and about 10 points per millimeter in the streamwise direction. For steady DNS, the domain is discretized using 4 points in the azimuthal direction, since the meanflow is axisymmetric. For unsteady DNS, the domain is discretized using 32 points in the azimuthal direction up to $s = 0.01$ m and 64 points between $s = 0.01$ m and $s = 0.2$ m. Based on the azimuthal spectrum of the freestream disturbances considered in this study, this azimuthal resolution should be sufficient to capture the physics of the 3-D receptivity process.

Table 1 Freestream conditions

Parameter	Value	Parameter	Value
M_∞	15	$H_{0,\infty}$	10.34 MJ/kg
ρ_∞	3.405×10^{-2} kg/m^3	p_∞	2188 Pa
T_∞	222.5 K	Re_1	10.5×10^6
Y_{N_2}	0.78	Y_{O_2}	0.22

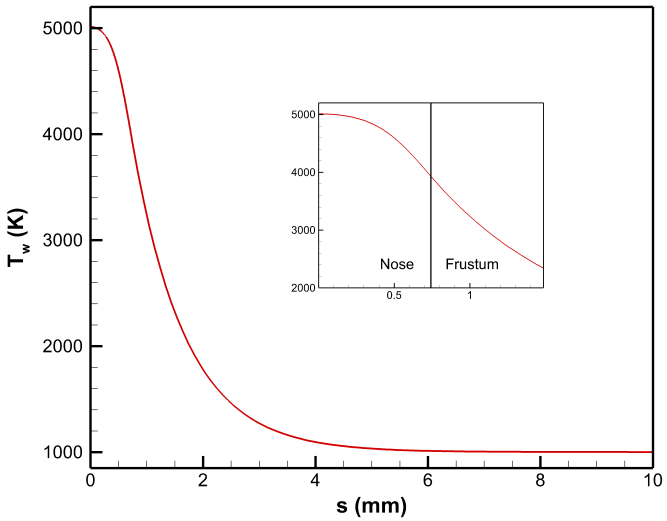

Fig. 1 Wall temperature variation versus streamwise distance

III. Governing Equations and Gas Model

The gas model is formulated for thermochemical nonequilibrium assuming a two-temperature model. The rotational mode is assumed to be fully excited and in equilibrium with the translation mode. Two temperatures are used to represent translation-rotation energy and vibration energy, respectively. The five species model (N_2, O_2, NO, N and O) is used to simulate air chemistry. The Navier-Stokes equations in conservative form consist of five species mass conservation equations, three momentum conservation equations, the total energy equation, and the vibration energy equation. The governing equations in vector form are written as

$$\frac{\partial U}{\partial t} + \frac{\partial F_j}{\partial x_j} + \frac{\partial G_j}{\partial x_j} = W \tag{1}$$

where U is the state vector of conserved quantities and W is the source terms defined by

$$U = \begin{bmatrix} \rho_1 \\ \vdots \\ \rho_{ns} \\ \rho u_1 \\ \rho u_2 \\ \rho u_3 \\ \rho e \\ \rho e_v \end{bmatrix}, \quad W = \begin{bmatrix} \omega_1 \\ \vdots \\ \omega_{ns} \\ 0 \\ 0 \\ 0 \\ 0 \\ \sum_{s=1}^{nms} \left(Q_{T-V,s} + \omega_s e_{v,s} \right) \end{bmatrix}.$$

The inviscid and viscous flux vectors, F_j and G_j, respectively, are defined by

$$F_j = \begin{bmatrix} \rho_1 u_j \\ \vdots \\ \rho_{ns} u_j \\ \rho u_1 u_j + p\delta_{1j} \\ \rho u_2 u_j + p\delta_{2j} \\ \rho u_3 u_j + p\delta_{3j} \\ (p + \rho e)\, u_j \\ \rho e_v u_j \end{bmatrix}$$

$$G_j = \begin{bmatrix} \rho_1 v_{1j} \\ \vdots \\ \rho_{ns} v_{nsj} \\ \tau_{1j} \\ \tau_{2j} \\ \tau_{3j} \\ -u_i \tau_{ij} - k_T \frac{\partial T}{\partial x_j} - k_V \frac{\partial T_V}{\partial x_j} + \sum_{s=1}^{nms} \rho_s h_s v_{sj} \\ -k_V \frac{\partial T_V}{\partial x_j} + \sum_{s=1}^{nms} \rho_s e_{v,s} v_{sj} \end{bmatrix}$$

where v_{sj} is the species diffusion velocity, and

$$\tau_{ij} = \mu \left(\frac{\partial u_i}{\partial x_j} + \frac{\partial u_j}{\partial x_i} \right) - \frac{2}{3} \mu \frac{\partial u_k}{\partial x_k} \delta_{ij} \tag{2}$$

is the viscous stress. The total energy per unit volume, ρe, is defined as

$$\rho e = \sum_{s=1}^{ns} \rho_s c_{v,s} T + \rho e_v + \frac{1}{2} \rho \left(u_1^2 + u_2^2 + u_3^2 \right) + \sum_{s=1}^{ns} \rho_s h_s^o \tag{3}$$

where h_s^o is the species heat of formation, $e_{v,s}$ is the species vibration energy, and $c_{v,s}$ is the species translation-rotation specific heat at constant volume, defined as

$$c_{v,s} = \begin{cases} \frac{5}{2} \frac{R}{M_s} & s = 1, 2, \ldots, nms \\ \frac{3}{2} \frac{R}{M_s} & s = nms + 1, \ldots, ns. \end{cases} \tag{4}$$

The vibration energy per unit volume, ρe_v, is defined as

$$\rho e_v = \sum_{s=1}^{nms} \rho_s e_{v,s} = \sum_{s=1}^{nms} \rho_s \frac{R}{M_s} \frac{\theta_{v,s}}{\exp\left(\theta_{v,s}/T_V\right) - 1} \tag{5}$$

where $\theta_{v,s}$ is the characteristic vibrational temperature of each vibrational mode. The characteristic vibration temperatures are taken from Park [5]. To model chemical nonequilibrium, three dissociation reactions and three exchange reactions are used. Each reaction is governed by a forward and backward reaction rate determined from

$$k_f = C_f T_a^{\eta} \exp\left(-\theta_d / T_a\right) \tag{6}$$

$$k_b = k_f / K_{eq} \tag{7}$$

where all forward reaction rates are obtained from Park [5]. The equilibrium coefficient, K_{eq}, is determined by using

$$K_{eq} = A_0 \exp\left(\frac{A_1}{Z} + A_2 + A_3 \ln(Z) + A_4 Z + A_5 Z^2 \right), \tag{8}$$

$$Z = \frac{10000}{T} \tag{9}$$

which is a curve fit to experimental data from Park [5].

The source term in the vibration energy equation representing the exchange of energy between the translation-rotation and vibration energies is calculated using the Landau-Teller formulation:

$$Q_{T-V,s} = \rho_s \frac{e_{v,s}(T) - e_{v,s}(T_V)}{< \tau_s > + \tau_{cs}} \tag{10}$$

where $< \tau_s >$ is the Landau-Teller relaxation time given by Lee [6]. The term τ_{cs} from Park [5] is used to more accurately model the relaxation time in areas of high temperatures occurring just downstream of the bow shock.

The viscosity of each species is computed using a Blottner curve fit shown in Eq. 11, with coefficients from Blottner *et al.* [7]. The mixture viscosity is found using Wilke's [8] mixing rule (Eq. 12-14). The overall heat conductivities for each energy mode are computed in a similar way. The diffusion velocity is calculated using Fick's law (Eq. 15) and a constant Schmidt number of 0.5 (Eq. 16).

$$\mu_s = 0.1 \exp\left[\left(A_s^\mu \ln(T) + B_s^\mu\right)\ln(T) + C_s^\mu\right] \tag{11}$$

$$\mu = \sum_{s=1}^{ns} \frac{X_s \mu_s}{\phi_s} \tag{12}$$

$$X_s = \frac{c_s}{M_s} \tag{13}$$

$$\phi_s = \frac{\sum_{r=1}^{ns} X_r \left[1 + \left(\frac{M_s}{M_r}\right)^{1/4}\right]^2}{\left[8\left(1 + \frac{M_s}{M_r}\right)\right]^{1/2}} \tag{14}$$

$$\rho_s v_{s,j} = -\rho D_s \frac{\partial c_s}{\partial x_j} \tag{15}$$

$$Sc = \frac{\mu}{\rho D} = 0.5 \tag{16}$$

IV. Numerical Methods

A. Direct Numerical Simulation (DNS)

This work uses the thermochemical nonequilibrium shock-fitting DNS code of Mortensen and Zhong [9–14]. This code is capable of simulating five-species or eleven-species thermochemical nonequilibrium flow. Since for shock-fitting computations, the shock location is not known *a priori*, its position is solved along with the flow field. Accordingly, the computational grid is also a function of time. This leads to the coordinate transformation of the governing conservation equations

$$\begin{cases} \xi = \xi(x,y,z) \\ \eta = \eta(x,y,z,t) \\ \zeta = \zeta(x,y,z) \\ \tau = t \end{cases} \iff \begin{cases} x = x(\xi,\eta,\zeta,\tau) \\ y = y(\xi,\eta,\zeta,\tau) \\ z = z(\xi,\eta,\zeta,\tau) \\ t = \tau \end{cases} \tag{17}$$

where ξ is in the streamwise direction, η is normal to the body, ζ is in the azimuthal direction, $\zeta_t = 0$, and $\xi_t = 0$. The governing equation can then be transformed into computational space as

$$\frac{1}{J}\frac{\partial U}{\partial \tau} + \frac{\partial E'}{\partial \xi} + \frac{\partial F'}{\partial \eta} + \frac{\partial G'}{\partial \zeta} + \frac{\partial E'_v}{\partial \xi} + \frac{\partial F'_v}{\partial \eta} + \frac{\partial G'_v}{\partial \zeta} + U\frac{\partial (1/J)}{\partial \tau} = \frac{W}{J} \tag{18}$$

where J is the Jacobian of the coordinate transformation and

$$E' = \frac{F_1 \xi_x + F_2 \xi_y + F_3 \xi_z}{J} \tag{19}$$

$$F' = \frac{F_1\eta_x + F_2\eta_y + F_3\eta_z}{J} \tag{20}$$

$$G' = \frac{F_1\zeta_x + F_2\zeta_y + F_3\zeta_z}{J} \tag{21}$$

$$E'_v = \frac{G_1\xi_x + G_2\xi_y + G_3\xi_z}{J} \tag{22}$$

$$F'_v = \frac{G_1\eta_x + G_2\eta_y + G_3\eta_z}{J} \tag{23}$$

$$G'_v = \frac{G_1\zeta_x + G_2\zeta_y + G_3\zeta_z}{J}. \tag{24}$$

A seven-point stencil is used to discretize the spatial derivatives

$$\frac{\partial f_i}{\partial x} = \frac{1}{hb_i}\sum_{k=-3}^{3}\alpha_{i+k}f_{i+k} - \frac{\alpha}{6!b_i}h^5\left(\frac{\partial f^6}{\partial^6 x}\right) \tag{25}$$

where

$$\alpha_{i\pm3} = \pm1 + \frac{1}{12}\alpha, \qquad \alpha_{i\pm2} = \mp9 - \frac{1}{2}\alpha$$

$$\alpha_{i\pm1} = \pm45 + \frac{5}{4}\alpha, \qquad \alpha_i = -\frac{5}{3}\alpha$$

$$b_i = 60$$

and where h is the step size, $\alpha < 0$ is a fifth order upwind explicit scheme, and $\alpha = 0$ reduces to a sixth order central scheme. Here the inviscid terms use $\alpha = -6$ which yields a low dissipation fifth-order upwinded difference and the viscous terms are discretized using $\alpha = 0$. The derivatives in the transverse direction, if required, are treated with Fourier collocation. Second derivatives are computed by applying the first-order derivative operator twice. Numerical tests indicated that, because of the absence of numerical dissipation in Fourier discretization, higher azimuthal wavenumber modes can grow unbounded, eventually destroying the solution. Therefore, it is necessary to filter the solution in the azimuthal direction, either through solution filtering, in which the solution is filtered after some fixed number of timesteps or through derivative filtering, in which the Fourier coefficients of the derivatives of the solution are modified. In this paper, the 24th-order exponential derivative filter of Pruett and Chang [15] is used.

The inviscid flux terms are treated using flux splitting,

$$F' = F'^{+} + F'^{-} \tag{26}$$

where

$$F'^{\pm} = \frac{1}{2}(F' \pm \Lambda U) \tag{27}$$

and Λ is a diagonal matrix that ensures F'^{+} and F'^{-} contain only pure positive and negative eigenvalues, respectively. For thermochemical nonequilibrium, the eigenvalues of Λ were derived by Liu and Vinokur [16].

A method-of-lines approach is then used to advance the solution in time. For steady-state computations, the forward Euler method is used to advance the solution. For unsteady computations, the 3rd-order Runge-Kutta method of Shu and Osher [17] is used. The flow conditions immediately behind the shock are calculated from the Rankine-Hugoniot relations. The chemical composition and vibrational energy in the freestream are frozen. The shock is assumed to be infinitely thin, such that there is a constant chemical composition and vibration temperature across the shock. A complete derivation of the thermochemical nonequilibrium shock fitting procedure can be found in the work of Mortensen [14].

B. Linear Stability Theory (LST)

The LST code used in this study uses the same 5-species thermochemical nonequilibrium gas model as the DNS code. This code was originally written by Mortensen [14] but was later expanded upon by Knisely [18]. The code partially relaxes the parallel mean flow assumption, and the mean flow wall-normal velocity is no longer assumed to be zero. In addition, the freestream shock boundary conditions developed by Knisely and Zhong [19] have been implemented.

The LST equations are derived from the Navier-Stokes equations by a perturbation expansion of the form $q = \overline{q} + q'$, where q represents the value of some flow quantity, $\overline{q}$ is the mean flow quantity, and q' is the perturbation quantity. The steady flow terms can then be removed under the assumption that they satisfy the governing equations themselves. The perturbation quantities are assumed to be small such that higher-order terms can be ignored. In addition, it is assumed that the mean flow is parallel, such that the mean flow terms are functions of y only. This is an appropriate assumption since gradients in the wall-normal direction are often negligible compared to gradients in the streamwise direction. The perturbation terms are then assumed to take the form of a normal mode such that $q' = \hat{q}(y) \exp\left[i\left(\alpha x + \beta z - \omega t\right)\right]$, where ω is the circular frequency of the disturbance and α and β are the wave numbers. Note that in this context, x, y, and z are *local* coordinates in the streamwise, wall-normal, and spanwise directions respectively, and should not be confused with the global coordinate system shown in Fig. 2. This study is concerned with spatial stability, and ω and β are real and specified *a priori*. In addition, α is assumed to be complex such that $\alpha = \alpha_r + i\alpha_i$. In spatial stability theory, α_r is the streamwise wave number, and $-\alpha_i$ is the growth rate. A positive value for $-\alpha_i$ corresponds to growth, whereas a negative value of $-\alpha_i$ corresponds to decay. Substituting the normal mode form of the perturbation quantity into the governing equations then yields a set of $ns + 5$ coupled ordinary differential equations of the form

$$\left(\mathbf{A}\frac{d^2}{dy^2} + \mathbf{B}\frac{d}{dy} + \mathbf{C}\right)\vec{\phi} = \vec{0}. \tag{28}$$

where $\vec{\phi} = \left[\hat{\rho}_1, \hat{\rho}_2, \ldots, \hat{\rho}_{ns}, \hat{u}, \hat{v}, \hat{w}, \hat{T}, \hat{T}_V\right]^T$, $\mathbf{A}$, $\mathbf{B}$ and $\mathbf{C}$ are complex square matrices of size $ns + 5$, and ns is the number of species in the gas model. Further details regarding the derivation of these matrices can be found in the work of Knisely [18].

C. Freestream Disturbance Model

The freestream vorticity disturbance is composed of planar waves, written as

$$\begin{bmatrix} u' \\ v' \\ w' \end{bmatrix}_\infty = \begin{bmatrix} \Delta u \\ \Delta v \\ \Delta w \end{bmatrix}_\infty \cos\left(k_x x + k_y y + k_z z - 2\pi f t + \psi\right) \tag{29}$$

where $(\,)'$ is the perturbation, $\Delta(\,)$ is the amplitude, k_x, k_y, and k_z are the wavenumbers in the axial (x), vertical (y) and spanwise (z) directions, f is the frequency, and ψ is the phase angle. Similarly to Schrader *et al.* [20], the disturbance is specified with the amplitude function and dispersion relation given by

$$\begin{bmatrix} \Delta u \\ \Delta v \\ \Delta w \end{bmatrix}_\infty = \frac{\epsilon u_\infty}{\sqrt{k_x^2 + k_y^2}} \begin{bmatrix} -k_y \\ k_x \\ 0 \end{bmatrix} \tag{30}$$

$$k_x = 2\pi f / u_\infty \tag{31}$$

where ϵ is the scale factor of the velocity perturbation vector and u_∞ is the steady freestream velocity, which is aligned with the axis of the cone. The square-root term in the denominator ensures that the amplitude of the wave is independent of k_x and k_y. In this study, we set $k_z = 0$, to reduce the computational workload through symmetry conditions on the y-axis. The computational setup associated with this disturbance is shown in Fig. 2.

The freestream disturbance is taken to be a superposition of three different vorticity waves with three different axial wavelengths, which correspond to frequencies of 400 kHz, 800 kHz, and 1200 kHz, via the dispersion relation. However, the vertical wavelength is set to the same value $\lambda_y = 10$ mm for each wave, corresponding to $k_y \approx 628$ m^{-1}. Since λ_y is the same for each wave, they all have similar azimuthal wavenumber spectra. For each wave, the phase angle is chosen randomly from a uniform distribution in the interval [0,2π]. The scale factor is chosen to be $\epsilon = 2 \times 10^{-6}$, so the disturbance is considered linear. Note that for a superposition of planar waves with different wavenumber vectors in 3-D space, it is difficult to eliminate local peaks where the amplitude exceeds that of each wave. Therefore, ϵ must be small enough so that the maximum amplitude of the overall disturbance (here it is $\epsilon_{max} = 6 \times 10^{-6}$) is also small enough to be considered linear.

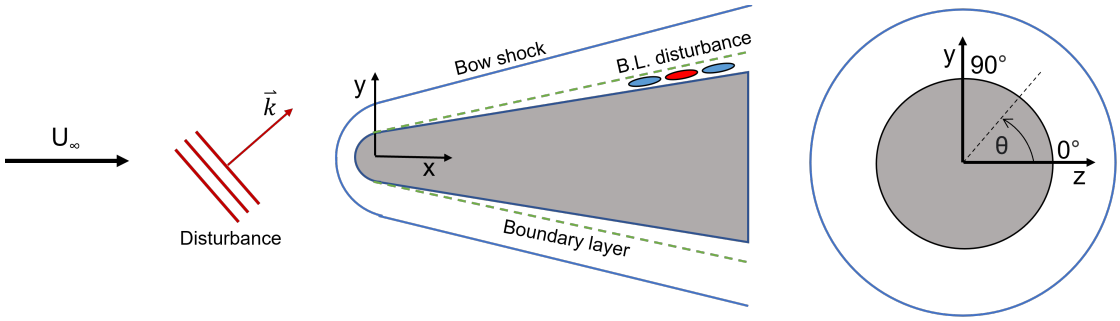

Fig. 2 Schematic of receptivity simulation setup (not to scale)

V. Steady DNS Results

The steady DNS results in the nose region are presented in Fig. 3. Here T is the translation-rotation (T-R) temperature and T_v is the vibration temperature. The highest translation-rotation temperatures are found near the stagnation line and towards the bow shock, reaching a maximum of about 9700 K. The wall temperature (both T and T_v) varies from 5500 K at the stagnation line to about 1900 K toward the end of the domain. There is a significant amount of thermal nonequilibrium (TNE) as indicated by the large differences between T and T_v throughout the flowfield. There is also a moderate amount of chemical nonequilibrium (CNE); the dissociation of O_2 into O causes the mass fraction of O to reach about 11% at the stagnation point. Although other reactions are present in the flowfield (creating NO and N, for example), the relatively high amounts of O mean that O_2 dissociation is the dominant reaction in the flowfield and that the mass fraction of O is an appropriate indicator of CNE.

Fig. 4 shows some typical mean flow profiles on the cone frustum, in this case, located at $s = 0.1$ m. TNE is still quite strong, as indicated by the large discrepancy between the profiles of T and T_v within the boundary layer; the maximum value of T is approximately 2400 K, whereas the maximum value of T_v is only about 1000 K. Since $T > T_v$, the vibration mode acts as an energy sink, absorbing energy from the T-R mode, and cooling the boundary layer compared to a perfect gas or a frozen gas. Knisely and Zhong [21] have shown that even in low Mach number flows at moderate stagnation enthalpy, TNE can have a substantial impact on stability; for cases where $T > T_v$, TNE can be destabilizing to the second mode, leading to larger growth rates and extended unstable regions. On the other hand, CNE is quite weak on the frustum (as indicated by the negligible amounts of O), so it is not expected to significantly affect second-mode stability. However, stronger CNE near the nose could still have a noticeable impact on the leading-edge receptivity process. Overall, the above results demonstrate the need to use a real-gas model in the present study.

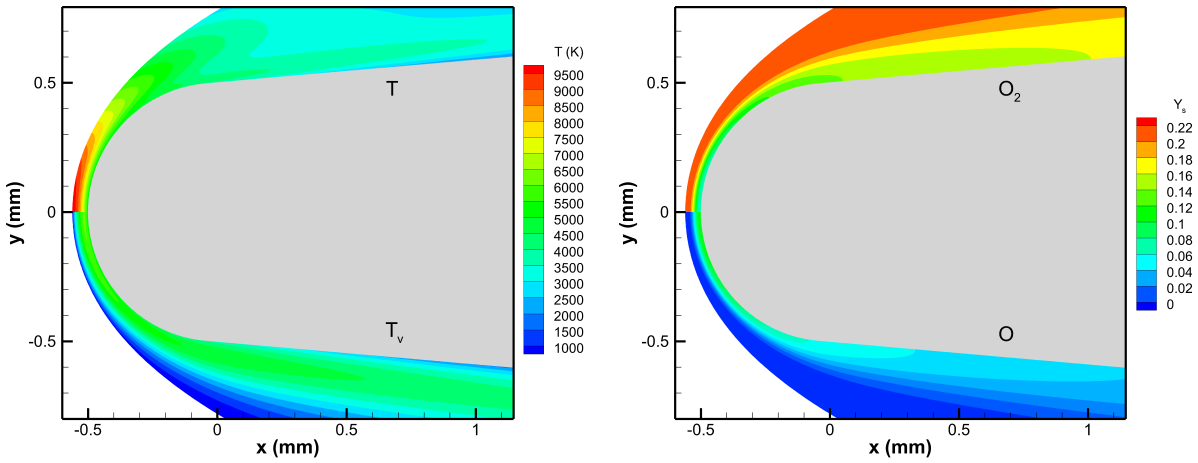

(a) (b)

Fig. 3 Contours of various quantities in the nose region, obtained from steady DNS. (a) Translation-rotation and vibration temperature. (b) Mass fraction of O_2 and O.

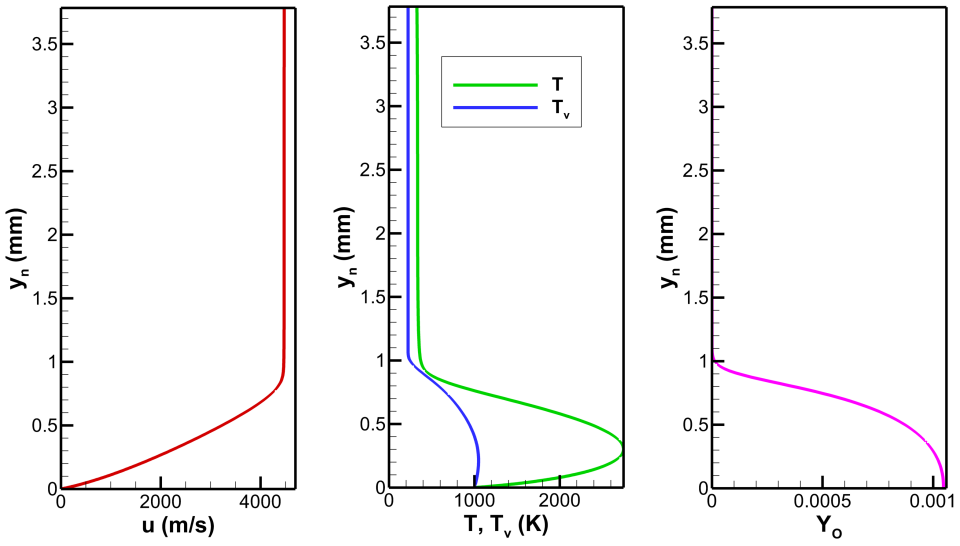

(a) (b) (c)

Fig. 4 Wall-normal profiles of various mean flow quantities at s = 0.1 m, obtained from steady DNS. (a) Wall-tangent velocity. (b) Translation-rotation and vibration temperatures. (c) Mass fraction of O.

VI. LST Results

Linear stability theory (LST) analysis was performed on the steady DNS mean flow to identify the unstable mode and its characteristics. Fig. 5 shows the streamwise behavior of the relevant 2-D discrete modes in terms of streamwise phase speed and growth rate at f = 400 kHz. The streamwise phase speed is calculated as $c_r = 2\pi f/\alpha_r$ and is non-dimensionalized by the post-shock wall-tangent velocity, u_{ps} = 4473 m/s. For future reference, k_c is the azimuthal wavenumber, i.e. the number of wavelengths around the circumference of the cone. Since the domain is periodic in the azimuthal direction, only integer values of k_c are physically consistent. For 2-D waves, k_c = 0. Mode S begins in the slow acoustic spectrum near the leading edge, but increases in phase speed downstream. Mode F_1^- begins in the fast acoustic spectrum near the leading edge but coalesces into the entropy/vorticity spectrum downstream, at which point a new mode, mode F_1^+, emerges [22]. This explains the jump in the growth rate as mode F_1^- crosses the entropy/vorticity spectrum. Mode S is second-mode unstable, as indicated by its destabilization near its synchronization with mode F_1^+.

A more complete view of the behavior of mode S can be obtained by looking at a stability map, as shown in Fig. 6. The contoured areas show the range of frequencies and streamwise locations at which mode S is unstable, and the growth rate is positive. The left-hand boundary of each of these regions is the branch I neutral point, where mode S first becomes unstable. The right-hand boundary is the branch II neutral point, where mode S becomes stable again. There is also a third-mode instability, associated with the synchronization of mode S with mode F_2^+ (a higher fast mode similar to mode F_1^+) and it occurs at a higher frequency range. However, in comparison to the second-mode instability, it has much smaller growth rates and occurs further downstream.

The likelihood of a given frequency to cause transition can be determined by using the N-factor method, where the N-factor is computed as

$$N(s) = \ln\left(\frac{A(s)}{A_0}\right) = \left[\int_{s_0}^{s} -\alpha_i(s)ds\right] \tag{32}$$

where A is the disturbance amplitude at some streamwise location downstream of the branch I neutral point, A_0 is the amplitude at the branch I neutral point (the initial amplitude), and s_0 is the location of the branch I neutral point. As can be seen, the N-factor is a measure of the amplitude ratio of the disturbance relative to its initial amplitude, with higher N-factors being more likely to lead to transition. It is well-known that the transition N-factor depends on the nature of the environmental disturbance, which varies from case to case. Free-flight transition N-factors are generally understood to be around 10 or more, whereas ground test N-factors can be much lower due to wind tunnel noise. Fig. 7 shows the N-factor envelope (the maximum N-factor attained out of all frequencies at a given streamwise location) for the 2-D second-mode instability. Interestingly, some of the higher frequencies (e.g. f = 1000 kHz) are both second-mode unstable and third-mode unstable and can achieve a larger N-factor (relative to the branch I neutral point of the second-mode instability) through third-mode amplification than through second-mode amplification alone. However, at any streamwise location, the maximum N-factor attained via third-mode amplification is smaller than that of second-mode amplification; as a result, the third-mode instability is unlikely to be relevant in terms of transition. The maximum N-factor attained within the domain considered is about 10, corresponding to second-mode amplification at f = 330 kHz (not shown).

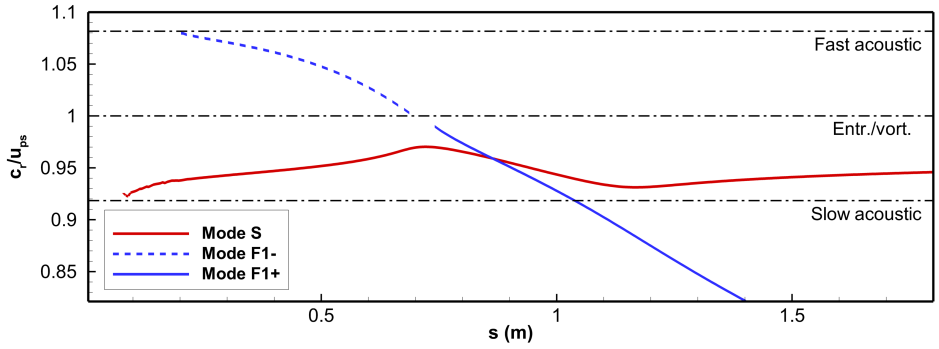

(a)

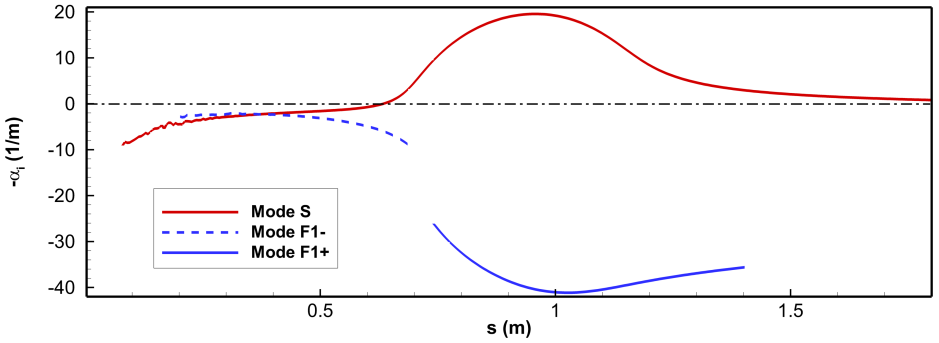

(b)

Fig. 5 Streamwise behavior of some 2-D discrete modes at f = 400 kHz, obtained from LST. (a) Streamwise phase speed. (b) Growth rate. The horizontal lines in the phase speed plot denote the phase speeds of the 2-D continuous spectra and are computed using the post-shock Mach number M_{ps} = 12.26.

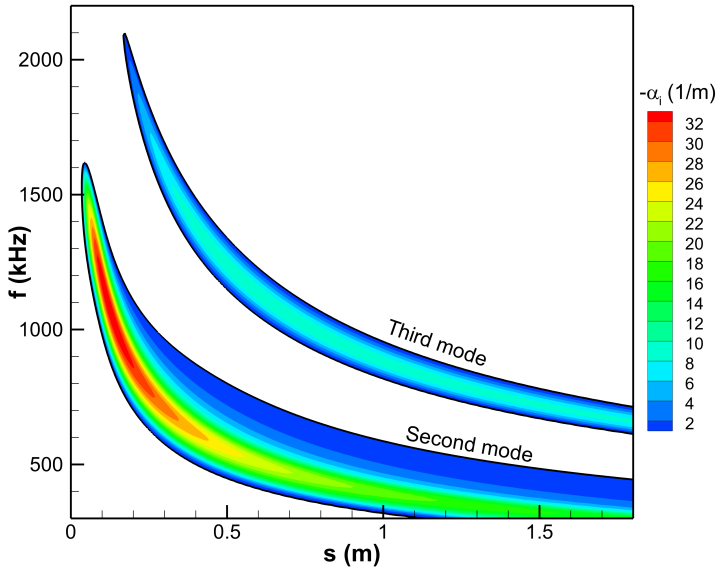

Fig. 6 Stability map for the 2-D mode S, obtained from LST. Only unstable regions are contoured.

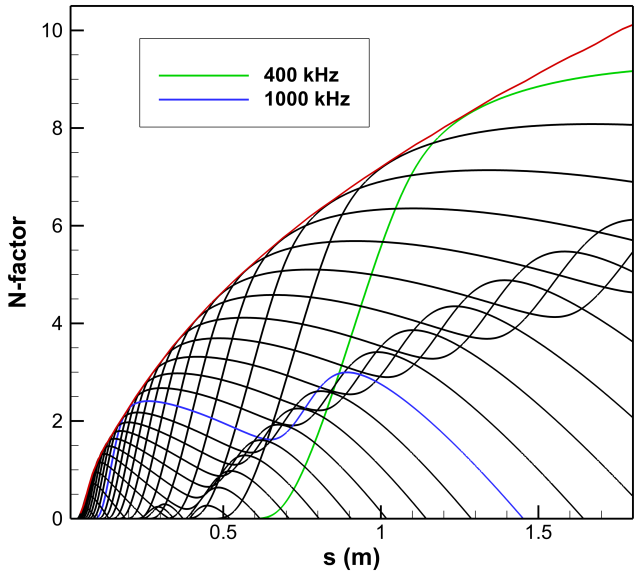

Fig. 7 2-D mode S N-factor curves and envelope, obtained from LST. The envelope (red line) corresponds to the N factors associated with the second-mode instability. Secondary peaks correspond to the third-mode instability. For frequencies that are both second-mode and third-mode unstable, the reference point is the second-mode branch I neutral point. Each curve is a different frequency in increments of Δf = 50 kHz.

VII. Unsteady DNS Results

In this section, we present the results of unsteady receptivity simulations involving the freestream vorticity disturbance described in section IV. Since the freestream disturbance is temporally periodic, the resulting unsteady flowfield can be analyzed via Fourier analysis. After the flowfield has reached a temporally periodic state (typically after 3-4 periods of the lowest imposed frequency), unsteady perturbation data are stored for one additional period, and a fast Fourier transform (FFT) is applied.

Fig. 8-10 show the contours of the Fourier reconstruction of the wall-pressure disturbance resulting from the freestream disturbance at each imposed frequency. Here, Fourier reconstruction refers to the reconstruction of the disturbance field at a given frequency using information obtained from FFT, using the following expression

$$p'(x, y, z, t) = \Delta p(x, y, z) \cos\left(\psi(x, y, z) - 2\pi f t\right) \tag{33}$$

where p' is the pressure perturbation, Δp is the amplitude (the magnitude of the complex FFT coefficient), and ψ is the phase angle. Here, p' is nondimensionalized by the freestream mean flow pressure (p_∞), and then normalized by the scale factor of the freestream disturbance (ϵ). The resulting expression can be written as $p'/(\epsilon p_\infty)$. It can be seen that the amplitude is much larger on the side of the cone facing away from the freestream disturbance (the leeward side) than on the side facing towards the freestream disturbance (the windward side). Note that the leeward side corresponds to azimuthal angles in the range $0^\circ < \theta < 180^\circ$ and the windward side corresponds to $180^\circ < \theta < 360^\circ$ (see Fig. 2). Wan *et al.* [3] found the same leeward-windward amplitude variation for oblique freestream slow acoustic waves. This variation can also be seen in the pressure perturbation amplitude behind the shock, which is shown in Fig. 11 for f = 800 kHz and s = 0.056 m. Looking at the leeward side of the f = 400 kHz and f = 800 kHz cases, there is some amplification upstream, which is attributed to the excitation of boundary layer modes through the leading-edge receptivity process (discussed later). In the f = 800 kHz and f = 1200 kHz cases, there is much stronger amplification further downstream, which is attributed to second-mode growth (also discussed later). Note that in the f = 1200 kHz case, the leading-edge receptivity region is somewhat obscured, as it is very close to the second-mode growth region, which begins very far upstream at this frequency. Lastly, there is a slight difference in streamwise wavelengths between the leeward and windward sides. The windward-to-leeward wavelength ratio seems to depend on the wave angle of the

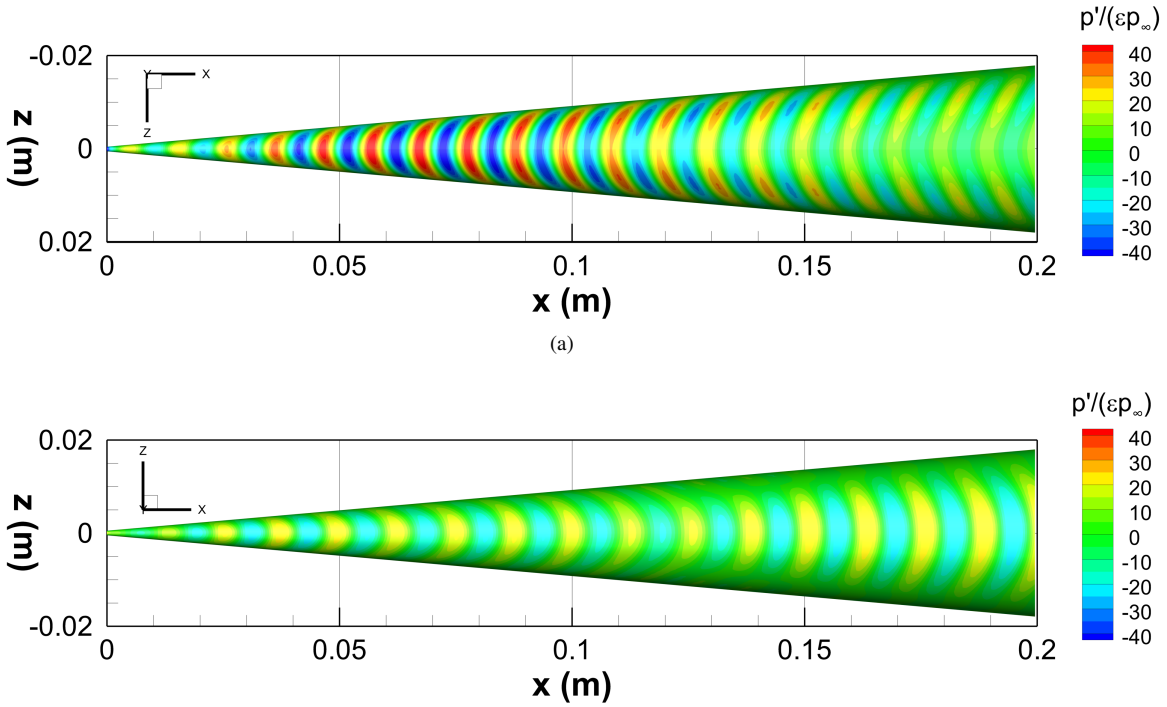

Fig. 8 Contours of the Fourier-reconstructed normalized wall-pressure perturbation $p'/(\epsilon p_\infty)$ at f = 400 kHz and t = 0 s, obtained from 1-D FFT of unsteady DNS. (a) Upper (leeward) side. (b) Lower (windward) side.

freestream disturbance, with a greater wave angle corresponding to a greater ratio, although there are likely other factors involved as well.

A. Disturbance Evolution at f = 400 kHz and f = 800 kHz

Fig. 12 and Fig. 13 show the streamwise variation of the wall-pressure amplitude for several values of k_c at f = 400 kHz and f = 800 kHz respectively. These curves are obtained by applying a 2-D FFT (in time and in the azimuthal direction) to the wall-pressure disturbance at each streamwise location on the surface. The amplitudes obtained from the FFT are then normalized in the same way as described before. Note that the azimuthal spectrum of the disturbance is symmetric about the k_c axis, so only positive values of k_c are shown, for brevity.

First, we provide a general overview of the receptivity process. The parametric effects of different azimuthal wavenumbers will be discussed later. In the leading-edge receptivity region (the region upstream of the second-mode branch I neutral point), the amplitude gradually increases with streamwise distance, leading to a maximum, and then gradually decreases with streamwise distance. For example, at f = 400 kHz and k_c = 0, the amplitude generally increases in the range of 0.006 m < s < 0.04 m, and then decreases, continuing downstream. It should be noted that these locations are quite rough and are meant as a guide only. The oscillations in amplitude are due to a modulation effect between modes; since the disturbance consists of multiple modes with differing phase speeds, there is constructive and destructive interference [23]. This also means that the amplitude curves here may not correspond exactly to the locations at which a particular mode, say mode S, amplifies or decays.

This amplification-decay behavior in the leading-edge receptivity region is related to the amplification-decay behavior of the boundary-layer discrete modes. Toward the leading edge, mode F_1^- and mode S are synchronized with the fast and slow acoustic continuous spectra, respectively, which allows these modes to be forced by fast and slow acoustic waves outside the boundary layer [24]. These fast and slow acoustic waves (as well as entropy and vorticity waves) originate from the interaction of the freestream vorticity disturbance with the shock [25]. Note that although both mode F_1^- and mode S undergo forcing, in many cases there is only one dominant receptivity mechanism, depending on the structure of the disturbance field in the shock layer. For example, Ma and Zhong [26] noted that for a Mach 4.5

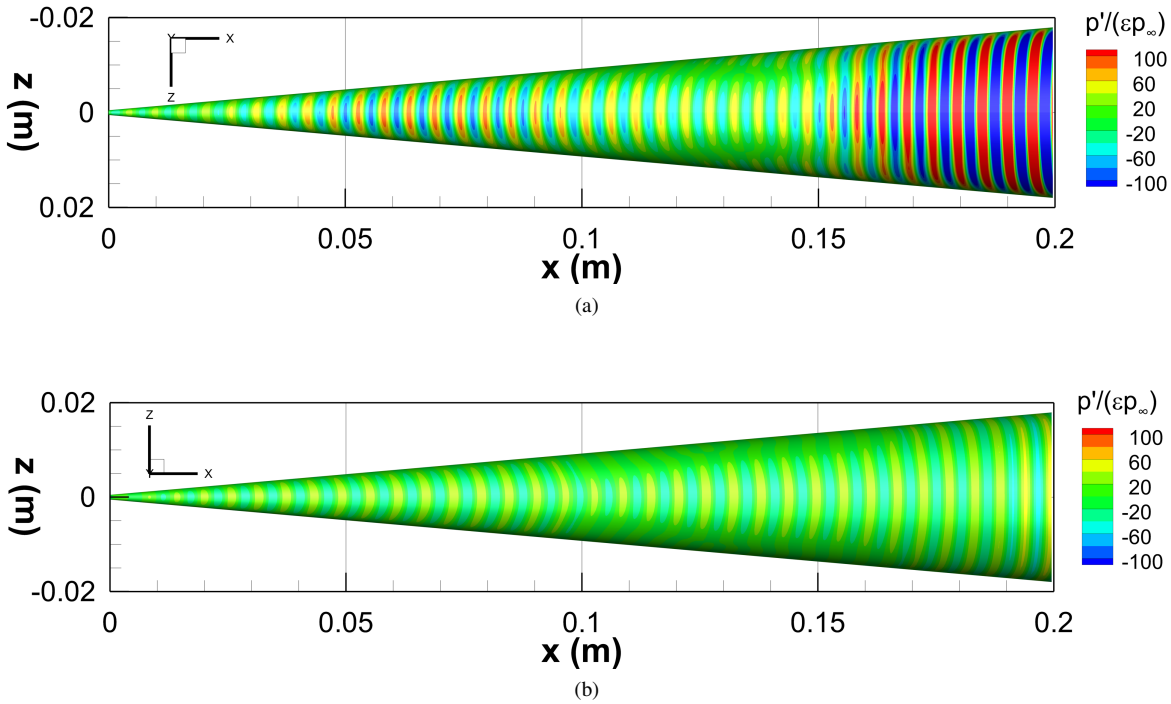

Fig. 9 Contours of the Fourier-reconstructed normalized wall-pressure perturbation $p'/(\epsilon p_\infty)$ at f = 800 kHz and t = 0 s, obtained from 1-D FFT of unsteady DNS. (a) Upper (leeward) side. (b) Lower (windward) side. The contour colors are cut off at ±100 to better illustrate the disturbance field.

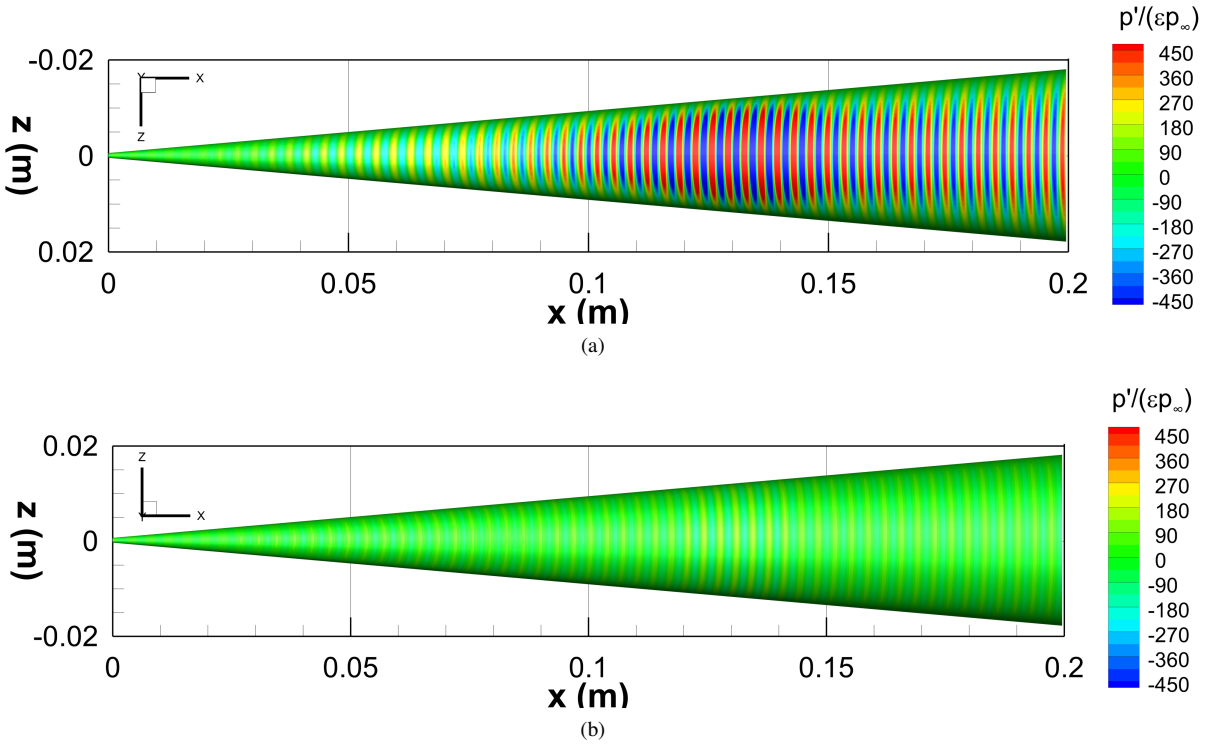

Fig. 10 Contours of the Fourier-reconstructed normalized wall-pressure perturbation $p'/(\epsilon p_\infty)$ at f = 1200 kHz and t = 0 s, obtained from 1-D FFT of unsteady DNS. (a) Upper (leeward) side. (b) Lower (windward) side. The contour colors are cut off at ±450 to better illustrate the disturbance field.

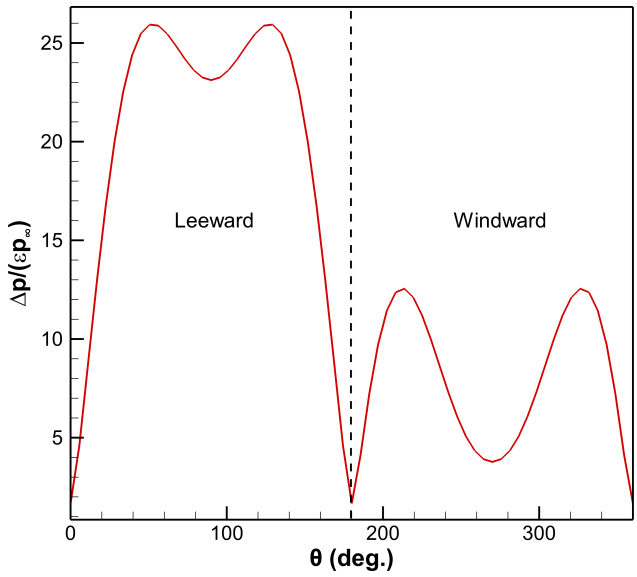

Fig. 11 Azimuthal variation of normalized pressure perturbation amplitude $\Delta p/(\epsilon p_\infty)$ immediately behind shock at s = 0.056 m and f = 800 kHz, obtained from 1-D FFT of unsteady DNS. The dashed line separates the leeward and windward sides (defined in the text).

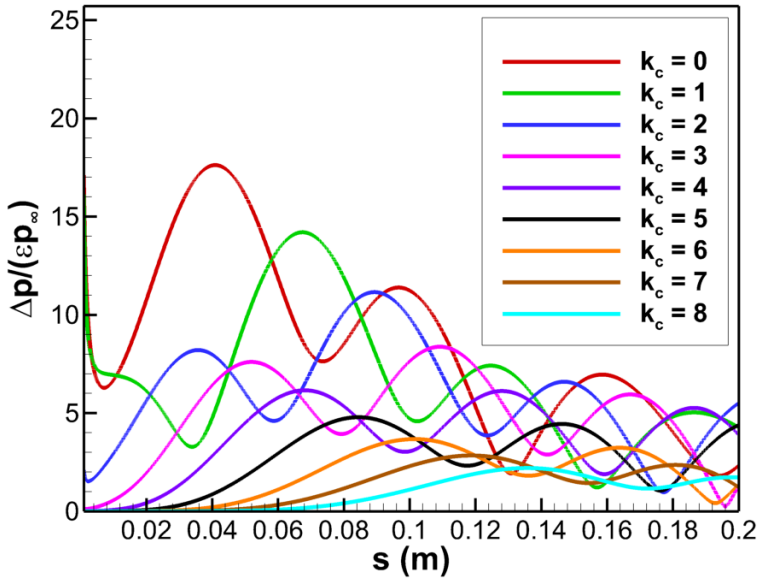

Fig. 12 Normalized wall-pressure perturbation amplitude $\Delta p/(\epsilon p_\infty)$ vs. streamwise distance for several azimuthal components at f = 400 kHz. Obtained from 2-D FFT of unsteady DNS at each streamwise location.

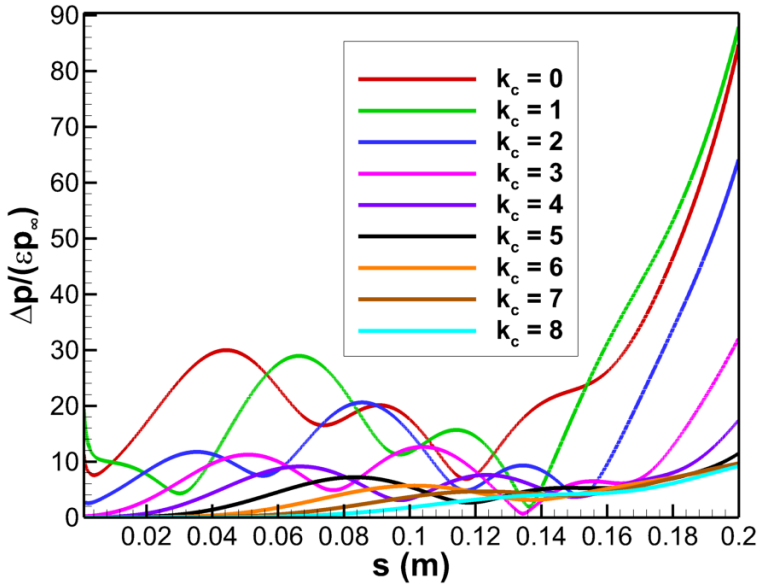

Fig. 13 Normalized wall-pressure perturbation amplitude $\Delta p/(\epsilon p_\infty)$ vs. streamwise distance for several azimuthal components at f = 800 kHz. Obtained from 2-D FFT of unsteady DNS at each streamwise location.

flat plate boundary layer, the dominant receptivity mechanism in the case of a freestream slow acoustic wave was the synchronization of mode S with slow acoustic forcing waves, while in the case of a freestream vorticity/entropy wave, the dominant receptivity mechanism was the synchronization of mode F_1^- with fast acoustic forcing waves. In the present case, the dominant mechanism is yet to be determined, so the discussion will proceed in general terms. The subsequent decrease in amplitude is because the otherwise-stable boundary-layer modes are no longer synchronized. Note that there is actually also a region where mode F_1^- and mode F_1^+ are synchronized with the entropy/vorticity spectrum (the c_r/u_{ps} = 1 line in Fig. 5), allowing these modes to be excited by forcing entropy or vorticity waves [27]. It remains to be seen whether this receptivity mechanism is significant for this flow.

The second-mode instability begins toward the end of the domain in Fig. 13 (f = 800 kHz), where a significant increase in amplitude is seen. This amplification can be confirmed to be due to the second-mode instability by comparing the location at which the amplitude appears to increase, to the branch I neutral point for that frequency. The LST results predict the neutral point to be around s = 0.15 m for the 2-D (k_c = 0) mode S. Indeed, the unsteady DNS results indicate that the 2-D mode grows substantially near this point, which confirms the second-mode instability. Note that no second-mode instability is seen for f = 400 kHz since it occurs much further downstream (see Fig. 5).

Note that in Fig. 12, for the k_c = 0 and k_c = 1 components, the amplitude is actually much higher in the nose region (not shown) but subsequently decays rapidly before increasing again due to forcing. This behavior was also noted by Cerminara [28], who attributed it to the strong amplification of waves when passing through the normal shock at the stagnation line. In other words, this behavior is not associated with the excitation of the discrete modes.

The streamwise amplitude curves for the oblique components ($k_c > 0$) show a qualitative behavior similar to that of the 2-D component in the leading-edge receptivity region. However, there are some key differences. One difference is the extended forcing region. This can be inferred by looking at the distance from the beginning of the domain to the location of maximum amplitude. For example, this distance is much greater for the k_c = 2 component when compared to the k_c = 0 component. This kind of observation breaks down for large k_c, since lower amplitudes are more susceptible to modulations, but the general trend should be the same. The extension of the forcing region for the oblique components may indicate that the oblique versions of mode F_1^- and mode S have a more extensive synchronization region with the fast and slow acoustic continuous spectra than the 2-D modes.

Another observation is that the oblique components overall have smaller amplitudes within the forcing region compared to the 2-D component. This is likely related, at least in part, to the local azimuthal content of the freestream disturbance, which varies according to the radial distance from the axis of the cone, and the vertical wavelength of the freestream disturbance. This idea is demonstrated by considering a simple model of a freestream velocity perturbation of the form

$$v' = \cos\left(k_y y\right) = \cos\left[2\pi\left(r/\lambda_y\right)\sin\theta\right] \tag{34}$$

where v' is the velocity perturbation in the vertical direction, r is the radial coordinate, and θ is the azimuthal coordinate (see Fig. 2). The radial component of this velocity perturbation can be written as

$$v'_r = \cos\left[2\pi\left(r/\lambda_y\right)\sin\theta\right]\sin\theta \tag{35}$$

From the above expression, we see that the azimuthal variation of this disturbance is characterized by the non-dimensional parameter r/λ_y. The azimuthal variation and spectrum of v'_r for several values of r/λ_y are shown in Fig. 14. Since the forcing waves originate from the shock-disturbance interaction, we can consider r to be the local shock radius (the distance from the cone axis to the shock). Near the leading edge, r/λ_y is very small, so the shock effectively sees a disturbance that has a very narrow azimuthal spectrum. As the shock radius increases moving downstream, the azimuthal spectrum broadens, and higher azimuthal modes emerge. This is reflected in the azimuthal wavenumber spectra of the pressure perturbation immediately behind the shock, shown in Fig. 15 for different streamwise locations at f = 800 kHz. It may be possible that in the forcing region, the forcing waves corresponding to that value of k_c are weaker than that of the 2-D wave, which would help explain the smaller overall amplitudes seen here for the oblique components. However, there are likely other factors to consider as well, so this explanation will need further study. Aside from the present case, the results also imply that the azimuthal wavenumber spectrum of a freestream disturbance with a fixed vertical wavelength will generally be much broader for a blunt-nose cone than a sharp-nose cone (due to the increase in shock radius), so consideration of oblique-mode receptivity may be particularly important in 3-D receptivity over blunt-nose cones.

It is interesting to note that in Figure 13 (f = 800 kHz), the k_c = 1 component is actually slightly larger in amplitude than that of the 2-D component. This may be the result of a weak first-mode instability or possibly a larger mode S amplitude at the second-mode branch I neutral point. The latter would need to be substantiated by isolating the amplitude of mode S via the methods discussed before.

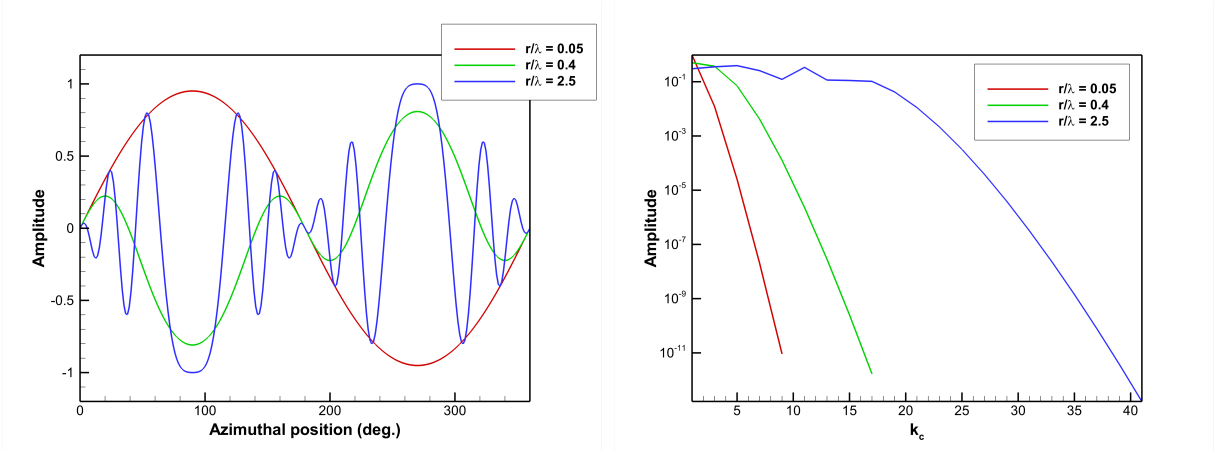

(a) (b)

Fig. 14 Characteristics of the simple freestream disturbance model (discussed in the text) for various values of r/λ_y (a) Amplitude vs. azimuthal position. (b) Amplitude vs. azimuthal wavenumber.

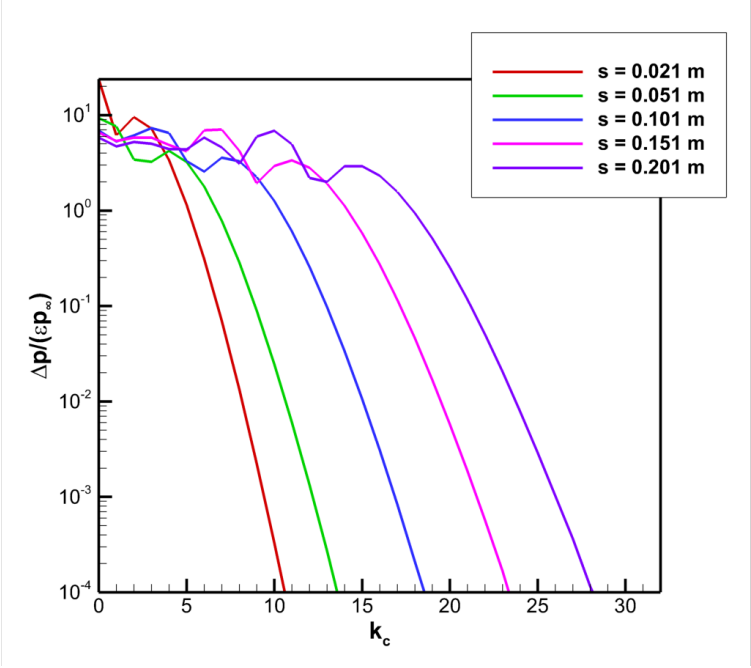

Fig. 15 Azimuthal spectrum of normalized pressure perturbation $\Delta p/(\epsilon p_\infty)$ immediately behind shock for various streamwise locations at f = 800 kHz

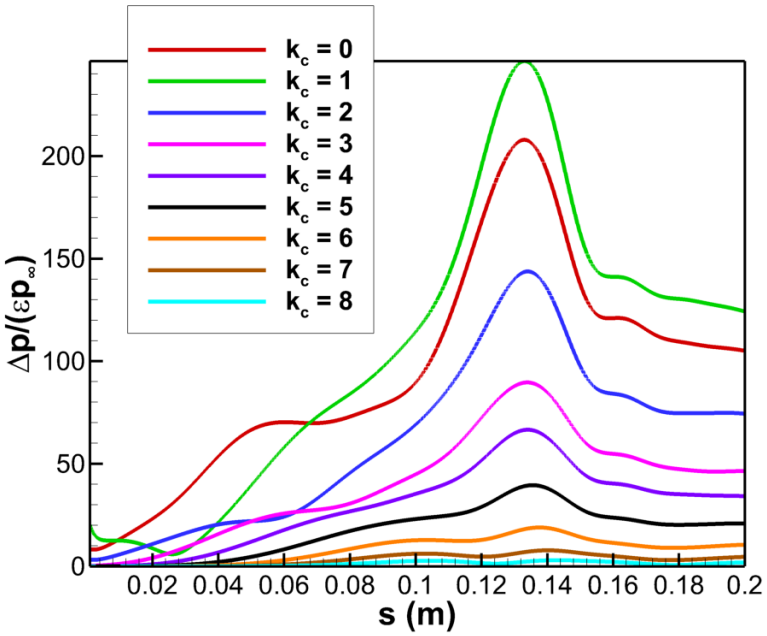

Fig. 16 Normalized wall-pressure perturbation amplitude $\Delta p/(\epsilon p_\infty)$ vs. streamwise distance for several azimuthal components at f = 1200 kHz. Obtained from 2-D FFT of unsteady DNS at each streamwise location.

B. Disturbance Evolution at f = 1200 kHz

The amplitude curves corresponding to f = 1200 kHz (Fig. 16) do not show the same distinct forcing/decay regions. Because second-mode growth is quite weak at this frequency (and the N-factors attained are very small), the second-mode instability region and leading-edge receptivity region appear to be merged together. There are non-parallel effects to consider as well. The oblique modes generally have lower amplitudes after second-mode growth. However, an interesting exception to this is the k_c = 1 component, which actually attains an amplitude greater than that of the 2-D component after second-mode amplification. As discussed in the f = 800 kHz case, this may be the result of a weak first-mode instability or a larger mode S amplitude at the second-mode branch I neutral point.

VIII. Conclusions

The three-dimensional linear receptivity of a Mach 15, axisymmetric straight cone boundary layer to an vorticity disturbance is investigated using thermochemical nonequilibrium direct numerical simulation (DNS) and linear stability theory (LST). LST results indicate that mode S is second-mode unstable. At the end of the domain (s = 1.8 m), the N-factor of the two-dimensional (2-D) mode S reaches a value of 10 through second-mode amplification. Unsteady DNS (up to s = 0.2 m) is performed to simulate the receptivity of the boundary layer to a freestream vorticity disturbance composed of three oblique planar vorticity waves, each with a different axial wavelength, corresponding to frequencies of 400 kHz, 800 kHz, and 1200 kHz, but the same vertical wavelength, which is set to 10 mm. The vertical wavelength is kept the same to ensure similar azimuthal wavenumber spectra. In the leading-edge receptivity region (upstream of second-mode amplification), for the waves corresponding to the two lower frequencies (400 kHz and 800 kHz), the results indicate an extended forcing region in the streamwise direction for the oblique components of the boundary-layer response when compared to the 2-D components. However, the oblique components also have smaller overall amplitudes within the forcing region compared to the 2-D component. For the wave corresponding to a frequency of 1200 kHz, similar observations could not be made, but the oblique components generally attain smaller amplitudes after second-mode growth in comparison to the 2-D component. Interestingly, the amplitude of the disturbance component corresponding to an azimuthal wavenumber of 1 surpasses that of the 2-D component after second-mode growth, although it is unknown at this point whether this would be true for the two lower frequencies. Future work involves continuation of unsteady DNS further downstream to analyze the evolution of the boundary-layer disturbance at 400 kHz and 800 kHz and obtaining mode S (second mode) receptivity coefficients, which will likely require LST N-factor

data for the oblique modes.

IX. Acknowledgments

This work was performed under the auspices of the U.S. Department of Energy by Lawrence Livermore National Laboratory (LLNL) under contract #DE-AC52-07NA27344. This work was also supported by LLNL under subcontract #B642550. Computational resources were provided by the Livermore Computing Center under LLNL subcontract #B642550. The views and conclusions contained herein are those of the authors and should not be interpreted as necessarily representing the official policies or endorsements, either expressed or implied, of the U.S. Department of Energy or the U.S. Government.

References

[1] Mack, L. M., "Boundary Layer Linear Stability Theory," Tech. rep., AGARD report No. 709, 1984.

[2] Balakumar, P., "Receptivity of Supersonic Boundary Layers Due To Acoustic Disturbances Over Blunt Cones," *37th AIAA Fluid Dynamics Conference and Exhibit*, 2007.

[3] Wan, B., Chen, J., Yuan, X., Hu, W., and Tu, G., "Three-Dimensional Receptivity of a Blunt-Cone Boundary Layer to Incident Slow Acoustic Waves," *AIAA Journal*, Vol. 60, No. 8, 2022, p. 4523–4531.

[4] Mortensen, C., "Toward an understanding of supersonic modes in boundary-layer transition for hypersonic flow over blunt cones," *Journal of Fluid Mechanics*, Vol. 846, 2018, pp. 789–814.

[5] Park, C., *Nonequilibrium Hypersonic Aerothermodynamics*, John Wiley & Sons Inc., New York, 1990.

[6] Lee, J., "Basic Governing Equations for the Flight Regimes of Aeroassisted Orbital Transfer Vehicles," *Thermal Design of Aeroassisted Orbital Transfer Vehicles*, Vol. 96, edited by H. F. Nelson, AIAA, 1985, pp. 3–53.

[7] Blottner, F., Johnson, M., and Ellis, M., "Chemically Reacting Gas Viscous Flow Program for Multi-Component Gas Mixtures," Tech. Rep. SC-RR–70-754, Sandia National Laboratories, 1971.

[8] Wilke, C., "A Viscosity Equation for Gas Mixtures," *The Journal of Chemical Physics*, Vol. 18, No. 4, 1950, pp. 517–519.

[9] Mortensen, C. H., and Zhong, X., "High-Order Shock-Fitting Method for Hypersonic Flow with Graphite Ablation and Boundary Layer Stability," *AIAA 2012-3150*, 2012.

[10] Mortensen, C. H., and Zhong, X., "Numerical Simulation of Graphite Ablation Induced Outgassing Effects on Hypersonic Boundary Layer Receptivity over a Cone Frustum," *AIAA 2013-0522*, 2013.

[11] Mortensen, C. H., and Zhong, X., "Real Gas and Surface Ablation Effects on Hypersonic Boundary Layer Instability over a Blunt Cone," *AIAA 2013-2981*, 2013.

[12] Mortensen, C. H., and Zhong, X., "Simulation of Second-Mode Instability in a Real-Gas Hypersonic Flow with Graphite Ablation," *AIAA Journal*, Vol. 52, No. 8, 2014, pp. 1632–1652.

[13] Mortensen, C. H., and Zhong, X., "Numerical Simulation of Hypersonic Boundary-Layer Instability in a Real Gas with Two-Dimensional Surface Roughness," *AIAA 2015-3077*, 2015.

[14] Mortensen, C. H., "Effects of Thermochemical Nonequilibrium on Hypersonic Boundary-Layer Instability in the Presence of Surface Ablation and Isolated Two-Dimensional Roughness," Ph.D. thesis, University of California Los Angeles, 2015.

[15] Pruett, D. C., and Chang, C.-L., "Spatial Direct Numerical Simulation of High-Speed Boundary-Layer Flows Part II: Transition on a Cone in Mach 8 Flow," *Theoretical and Computational Fluid Dynamics*, Vol. 7, 1995, pp. 397–424.

[16] Liu, Y., and Vinokur, M., "Nonequilibrium Flow Computations. I. An Analysis of Numerical Formulations of Conservation Laws," *Journal of Computational Physics*, Vol. 83, No. 2, 1989, pp. 373–397.

[17] Shu, C.-W., and Osher, S., "Efficient implementation of essentially non-oscillatory shock-capturing schemes," *Journal of Computational Physics*, Vol. 77, No. 2, 1988, pp. 439–471.

[18] Knisely, C., "Supersonic Unstable Modes in Hypersonic Boundary Layers with Thermochemical Nonequilibrium Effects," Ph.D. thesis, University of California, Los Angeles, 2018.

[19] Knisely, C., and Zhong, X., "An Investigation of Sound Radiation by Supersonic Unstable Modes in Hypersonic Boundary Layers," *AIAA 2017-4516*, 2017.

[20] Schrader, L.-U., Brandt, L., Mavriplis, C., and Henningson, D., "Receptivity to free-stream vorticity of flow past a flat plate with elliptic leading edge," *Journal of Fluid Mechanics*, Vol. 653, 2010, pp. 245–371.

[21] Knisely, C., and Zhong, X., "Impact of Vibrational Nonequilibrium on the Supersonic Mode in Hypersonic Boundary Layers," *AIAA Journal*, Vol. 58, No. 4, 2019.

[22] Fedorov, A., and Tumin, A., "High-speed boundary-layer instability: old terminology and a new framework," *AIAA Journal*, Vol. 49, No. 8, 2011, pp. 1647–1657.

[23] Zhong, X., and Ma, Y., "Boundary-layer receptivity of Mach 7.99 flow over a blunt cone to free-stream acoustic waves," *Journal of Fluid Mechanics*, Vol. 556, 2006, pp. 55–103.

[24] Fedorov, A., and Khokhlov, A., "Prehistory of Instability in a Hypersonic Boundary Layer," *Theoretical and Computational Fluid Dynamics*, Vol. 14, 2001, pp. 359–375.

[25] McKenzie, J. F., and Westphal, K. O., "Interaction of Linear Waves with Oblique Shock Waves," *The Physics of Fluids*, Vol. 11, No. 11, 1968.

[26] Ma, Y., and Zhong, X., "Receptivity of a supersonic boundary layer over a flat plate. Part 3. Effects of different types of free-stream disturbances," *Journal of Fluid Mechanics*, Vol. 488, 2003, pp. 31–78.

[27] Fedorov, A., and Tumin, A., "Initial-Value Problem for Hypersonic Boundary-Layer Flows," *AIAA Journal*, Vol. 41, No. 3, 2003, pp. 379–389.

[28] Cerminara, A., "Boundary-Layer Receptivity and Breakdown Mechanisms for Hypersonic Flow over Blunt Leading-Edge Configurations," Ph.D. thesis, University of Southampton, June 2017.